Title

Designing Optimal Perovskite Structure for High Ionic Conduction

Journal

Advanced Materials, 32(1)

ISSN

0935-9648

Authors

Gao, Ran

Jain, Abhinav CP

Pandya, Shishir

et al.

Publication Date

2020

DOI

10.1002/adma.201905178

Peer reviewed

Designing Optimal Perovskite Structure for High Ionic Conduction

*Ran Gao, Abhinav C. P. Jain, Shishir Pandya, Yongqi Dong, Yakun Yuan, Hua Zhou, Liv R. Dedon, Vincent Thoréton, Sahar Saremi, Ruijuan Xu, Aileen Luo, Ting Chen, Venkatraman Gopalan, Elif Ertekin, John Kilner, Tatsumi Ishihara, Nicola H. Perry, Dallas R. Trinkle, and Lane W. Martin**

Solid-oxide fuel/electrolyzer cells are limited by a dearth of electrolyte materials with low ohmic loss and an incomplete understanding of the structure–property relationships that would enable the rational design of better materials. Here, using epitaxial thin-film growth, synchrotron radiation, impedance spectroscopy, and density-functional theory, the impact of structural parameters (i.e., unit-cell volume and octahedral rotations) on ionic conductivity is delineated in $La_{0.9}Sr_{0.1}Ga_{0.95}Mg_{0.05}O_{3-\delta}$. As compared to the zero-strain state, compressive strain reduces the unit-cell volume while maintaining large octahedral rotations, resulting in a strong reduction of ionic conductivity, while tensile strain increases the unit-cell volume while quenching octahedral rotations, resulting in a negligible effect on the ionic conductivity. Calculations reveal that larger unit-cell volumes and octahedral rotations decrease migration barriers and create low-energy migration pathways, respectively. The desired combination of large unit-cell volume and octahedral rotations is normally contraindicated, but through the creation of superlattice structures both expanded unit-cell volume and large octahedral rotations are experimentally realized, which result in an enhancement of the ionic conductivity. All told, the potential to tune ionic conductivity with structure alone by a factor of ≈2.5 at around 600 °C is observed, which sheds new light on the rational design of ion-conducting perovskite electrolytes.

The need for high operation temperatures (>800 °C) for electrolyte-supported solid-oxide fuel/electrolyzer cells to reduce ohmic loss has been one of the major limitations for commercialization.[1–3] In an effort to push the operating temperature down to a more cost-effective range (<500 °C), considerable research activities have been undertaken on the development of electrolytes with improved low-temperature ionic conductivity.[4,5] In this regard, doped-perovskite systems (i.e., $A_{1-x}A'_xB_{1-y}B'_yO_{3-\delta}$ where A' and B' are aliovalent dopants) have emerged as promising candidates for oxygen-ion conductors. For example, strontium and magnesium co-doped $LaGaO_3$ has been identified as an excellent alternative to yttria-stabilized zirconia due to its competitive ionic conductivity (>0.01 S cm^{-1} at 600 °C) and chemical stability.[6–8] But, despite these attractive properties, few high-performance alternatives have been discovered[9,10] and a systematic approach to the design of such materials has yet to

Dr. R. Gao, Dr. S. Pandya, L. R. Dedon, Dr. S. Saremi, Dr. R. Xu, A. Luo, Prof. L. W. Martin
Department of Materials Science and Engineering
University of California
Berkeley, CA 94720, USA
E-mail: lwmartin@berkeley.edu

Dr. R. Gao, Dr. S. Pandya, L. R. Dedon, Dr. S. Saremi, Dr. R. Xu, A. Luo, Prof. L. W. Martin
Materials Sciences Division
Lawrence Berkeley National Laboratory
Berkeley, CA 94720, USA

Dr. A. C. P. Jain, Prof. D. R. Trinkle
Department of Materials Science and Engineering
University of Illinois
Urbana-Champaign
Urbana, IL 61081, USA

Dr. A. C. P. Jain, Prof. D. R. Trinkle
Materials Research Laboratory
University of Illinois
Urbana-Champaign
Urbana, IL 61081, USA

Y. Dong, Dr. H. Zhou
X-ray Science Division
Advanced Photon Source
Argonne National Laboratory
Argonne, IL 60439, USA

Y. Dong, Dr. H. Zhou
National Synchrotron Radiation Laboratory and CAS Key Laboratory of Materials for Energy Conversion
University of Science and Technology of China
Hefei, Anhui 230026, P. R. China

Dr. Y. Yuan, Prof. V. Gopalan
Department of Materials Science and Engineering
Pennsylvania State University
State College, PA 16802, USA

be established. This is made more difficult by the fact that most research has focused on polycrystalline and mesostructured ceramics wherein complexity arising from grain boundaries, twinning structures, secondary phases, etc., can make interpretation of results more challenging.[11–15] In turn, many of the advances have come from the chemical and physical intuitions of researchers in the field and time-consuming trial-and-error experimental iterations.

In order to advance a rational-design approach for ionic-conducting materials, it is vital to gain a thorough understanding of the impact of systematic changes to the structure and chemistry on property evolution. In this spirit, researchers have undertaken a range of studies on thin-film versions of various ionic-conducting systems where lattice symmetry, microstructure, and material stoichiometry can be deterministically controlled and studied.[16–20] At the same time, advances in theoretical understanding of these systems have provided suggestions as to how to manipulate the structure to improve vacancy migration.[21–24] These studies, however, have provided, at times, conflicting recommendations and outcomes. Such incongruous results are potentially related to incomplete or limited structural characterization of the systems under study and from confounding contributions arising from sample geometry/structure (e.g., microstructure[15,19] and substrate contributions to conductivity[20,25]). Additionally, most experimental studies have focused on fluorite structures while there have been limited studies (generally focused on chemical effects) in the more complex perovskite systems.[26,27] Thus, one opportunity to develop a rational-design approach for high ion-conducting perovskites is to quantitatively and deterministically control the structural variables and build up a systematic correlation between these variables and transport properties without convolution from such confounding effects.

Here, we create a model perovskite ion-conducting system using thin-film epitaxy where chemical inhomogeneity, grain boundaries, and secondary phases are absent. This multi-faceted experimental and theoretical study delineates the impact of structural parameters (namely, unit-cell volume and octahedral rotations) on ionic conductivity in the electrolyte $La_{0.9}Sr_{0.1}Ga_{0.95}Mg_{0.05}O_{3-\delta}$ (LSGM). Films were grown on a range of substrates producing strain states from –1.12% to 1.10%. As compared to the zero-strain (or bulk-like) state, compressive strain reduces the unit-cell volume while maintaining large octahedral rotations, whereas tensile strain increases the unit-cell volume while quenching octahedral rotations. In turn, compressive and tensile strains are found to strongly reduce and have negligible effect, respectively, on the ionic conductivity. The resulting intuitive design recommendation is that both large unit-cell volume and octahedral rotations are required for large ionic conductivity. Density-functional theory (DFT) calculations reveal that larger unit-cell volumes and octahedral rotations decrease migration-energy barriers and create a set of low-energy migration pathways, respectively. Unit-cell volume and octahedral rotations are strongly coupled and often contraindicated, but this limitation can be overcome via superlattice structuring that enables the creation of both large unit-cell volumes and octahedral rotations, which drives a subsequent enhancement of the ionic conductivity by a factor of ≈2.5 as compared to the compressively strained heterostructures. Ultimately, these findings provide a strong indication of the structure–transport relationships in the perovskite system and shed new light on how one can rationally design novel high-performance electrolytes.

100 nm LSGM/$NdGaO_3$ (110), $SrTiO_3$ (001), and $DyScO_3$ (110) heterostructures were grown via pulsed-laser deposition (PLD; Experimental Section) corresponding to lattice mismatches of –1.12%, +0.05%, and +1.10%, respectively (where "–" and "+" indicate compressive and tensile strain, respectively). The resulting $(001)_{pc}$-oriented heterostructures (where pc refers to pseudocubic indices) are found to be single phase and highly crystalline (Figure S1a, Supporting Information). Reciprocal space mapping studies (Experimental Section) of the LSGM heterostructures along two orthogonal in-plane directions reveal that the films are coherently strained on all substrates (**Figure 1**a and Figure S1b,c, Supporting Information). The stoichiometry of the films was characterized via Rutherford backscattering spectrometry (RBS; Experimental Section) and the film chemistries were found to be $La_{0.9}Sr_{0.1}Ga_{0.95}Mg_{0.05}O_{3-\delta}$ (Figure S1d, Supporting Information). The film stoichiometry is further supported by X-ray studies and extraction of lattice parameters (Figure S1e, Supporting Information). All told, the LSGM heterostructures are of the same chemistry and coherently strained to the various substrates.

Synchrotron-based half-order Bragg peak analysis (Experimental Section) is applied to further examine the octahedral rotation evolution under epitaxial constraint. Briefly, the octahedral rotations in a perovskite unit-cell decrease the lattice symmetry and give rise to half-order diffraction peaks of which the intensities are related to the magnitudes of the oxygen-anion and *A*- and *B*-cation displacements. For instance, a representative 1/2 1/2 3/2-diffraction peak for the LSGM/$SrTiO_3$ (001) heterostructure is shown (at 25 and 650 °C), indicating that octahedral rotations are present in the system and that the magnitude of the rotation is similar across the temperature range of our studies (Figure 1b). In turn, systematic fitting of characteristic half-order Bragg peak intensities (Figure S2, Supporting Information) reveals the angles by which the octahedra rotate along each orthogonal direction (i.e., α, β, and γ along $[100]_{pc}$, $[010]_{pc}$, and $[001]_{pc}$, respectively).[28–30] Thus, from both the reciprocal space mapping and half-order Bragg peak analysis studies, the structural parameters of the LSGM heterostructures and corresponding changes induced by epitaxial strain can be

Dr. V. Thoréton, Prof. T. Ishihara, Prof. N. H. Perry
WPI International Institute for Carbon-Neutral Energy Research (WPI-I2CNER)
Kyushu University
Fukuoka 819-0395, Japan
Dr. T. Chen
Department of Hydrogen Energy Systems
Kyushu University
Fukuoka 819-0395, Japan
Prof. E. Ertekin
Mechanical Science and Engineering
University of Illinois
Urbana-Champaign
Urbana, IL 61081, USA
Prof. J. Kilner
Department of Materials
Imperial College London
London SW72AZ, UK

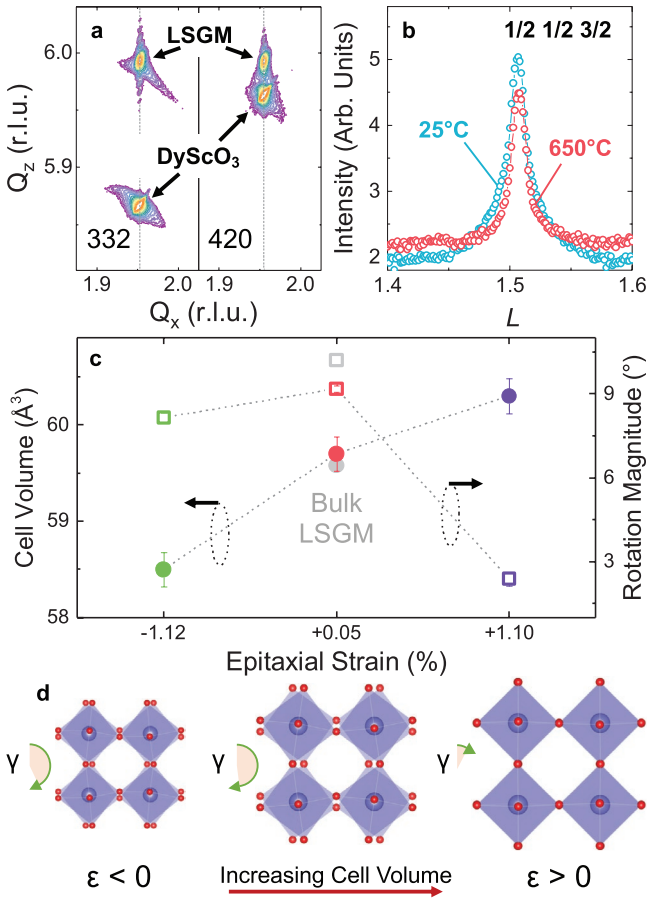

Figure 1. Structural characterization of $La_{0.9}Sr_{0.1}Ga_{0.95}Mg_{0.05}O_{3-\delta}$ (LSGM) thin films. a) Representative reciprocal space mapping studies from an LSGM/$DyScO_3$ heterostructure with maps along two orthogonal directions, confirming that the film is coherently strained to the substrate. b) Representative half-order Bragg peaks, in this case 1/2 1/2 3/2 peaks taken at 25 and 650 °C, which can be used to extract octahedral rotation pattern/angles. c) Extraction of the unit-cell volume (left axis, filled circles) and the effective octahedral rotation magnitude (right axis, open squares) as a function of strain state. d) Schematic illustration of the evolution of the LSGM structure with varying strain; note that the oxygen positions are extracted from X-ray studies while the octahedral rotation magnitude has been exaggerated for better representation.

extracted (Figure 1c and Table S1, Supporting Information). For simplicity of presentation, in later discussions we define an effective octahedral rotation magnitude as $\sqrt{\alpha^2+\beta^2+\gamma^2}$. To summarize the observations, in comparison to the zero-strain state (i.e., on $SrTiO_3$ substrates, where the extracted structural parameters are in agreement with bulk[31–33]), as we progress from compressive to tensile strain, the unit-cell volume of LSGM increases monotonically. Additionally, while the octahedral rotations are found to be the largest near the zero-strain state, they are slightly quenched under compressive strain, and almost fully suppressed under tensile strain (Figure 1d where a projection of the structure along the $[001]_{pc}$ is shown).

With this understanding of the structural evolution, we proceed to correlate these structural changes with the ion transport. To characterize ion-transport properties in the films, in-plane AC-impedance spectroscopy measurements are performed on all heterostructures from 500 to 650 °C under high (pure O_2) and low (pure N_2) oxygen-partial pressures (Experimental Section). The temperature region is purposely chosen to limit both the ionic and electronic contributions of the substrate to the overall measured conductivity (Supporting Information). For brevity, representative Nyquist plots, taken at 500 °C, are provided (**Figure 2**a–c), but data across the full measured temperature range are available (Figure S3a–c, Supporting Information). All heterostructures show one dominant "waterdrop-like" feature, characteristic of a mixed ionic and electronic conductor with ionic blocking boundary conditions. Thus, the high-frequency intercept gives the total resistance ($R_{total} = R_i + R_e$, where R_i and R_e are the ionic and electronic resistance, respectively), while the low-frequency intercept gives the electronic resistance and the electrode impedance.[34,35] Since the low-frequency resistance increases at lower oxygen-partial pressure and the triple-phase boundary area in dense platinum electrodes is small, this suggests that there is limited p-type electronic conduction in the LSGM films. The invariant high-frequency resistance under different oxygen-partial pressures suggests that the ionic-charge concentration is independent of gas environment and fixed by extrinsic dopants. This means that the conduction in the heterostructures predominantly arises from the LSGM films, not the substrates. To further rule out substrate contributions, measurements on bare substrates were also performed (Figure S4a–c, Supporting Information). The $NdGaO_3$ and $DyScO_3$ substrates show negligible mixed ionic and electronic conductance while the $SrTiO_3$ substrates show dominant p-type electronic conduction, which will not affect the ionic conduction extracted from the heterostructures.[36]

The ionic conductivity of the LSGM is determined by fitting the impedance spectra using a transmission-line model developed for mixed ionic and electronic conductors (Figure S5a–c, Supporting Information). Fitting reveals a high transference number ($t = \frac{\sigma_T - \sigma_e}{\sigma_T}$, where σ_T and σ_e are the total and electronic conductivity, respectively) of 0.94–0.98 across all heterostructures (Figure 2d), consistent with results for LSGM single crystals.[8] The smaller transference number in the LSGM/$SrTiO_3$ heterostructures is expected due to the relatively high electronic conduction from the substrates. In turn, we can extract the strain and temperature-dependent evolution of the ionic conductivity and the migration-energy barrier for all heterostructures (Figure 2e). Examination of the conductivity and the structural parameters reveals several key findings. First, the activation energy of conduction is found to be within the range of E_a = 0.65–0.75 eV for all heterostructures. It should be noted that due to the relatively small temperature window used to extract the activation energy of conduction (which was intended to limit the substrate contributions to overall conductivity), one cannot resolve a difference in the activation energy of conduction smaller than ≈0.1 eV. This is further compounded by the nonlinear nature of activation energy in LSGM around 500 °C.[8] Wider-temperature-range measurements, excluding LSGM/$SrTiO_3$ heterostructures wherein the substrate contributes too much to ionic conduction to allow for reliable extraction of the real conductivity of the LSGM, were completed for the LSGM/$NdGaO_3$ and $DyScO_3$ heterostructures and revealed a change of the activation energy of conduction of ≈0.12 eV from compressive to tensile strains (Figure S6, Supporting Information).

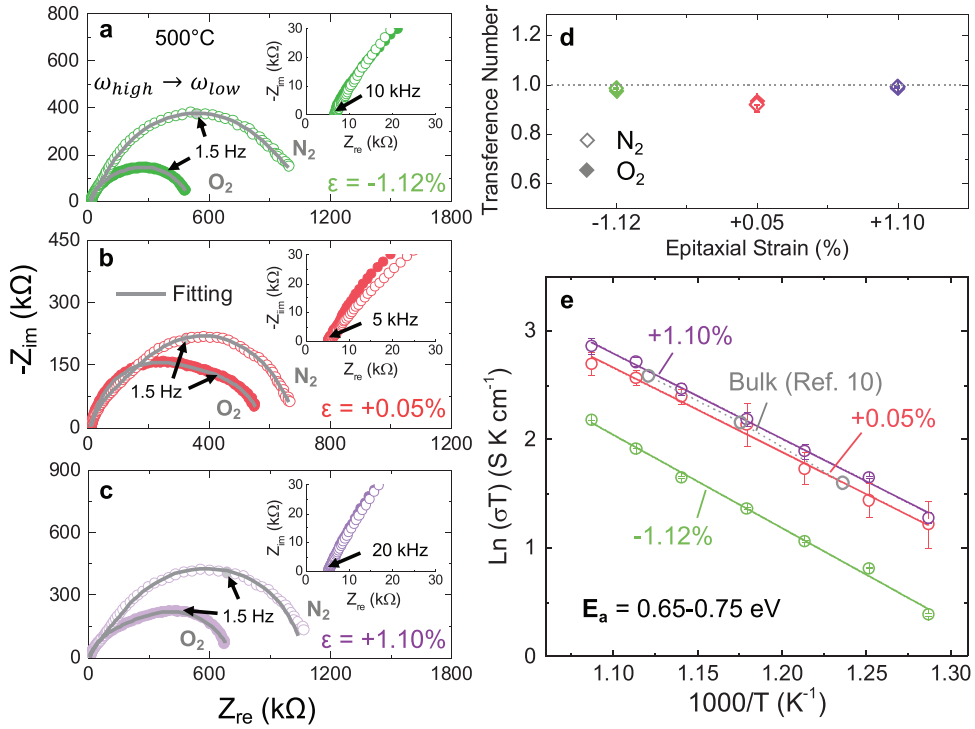

Figure 2. Ion-transport studies of LSGM thin films. a–c) Impedance spectra taken at 500 °C in both pure oxygen (filled circles) and nitrogen (open circles) for LSGM films grown on $NdGaO_3$ ($\varepsilon = -1.12\%$) (a), $SrTiO_3$ ($\varepsilon = 0.05\%$) (b), and $DyScO_3$ ($\varepsilon = 1.10\%$) (c) substrates. The total impedance (high-frequency intercept) is orders of magnitude lower than the electronic impedance (low-frequency intercept) and is independent of oxygen partial pressure (inset). d) Extracted transference numbers as a function of strain state agree well with single-crystal data. e) Arrhenius plot of the LSGM conductivity as a function of strain and temperature. The activation energies for oxygen vacancy migration for all heterostructures are ≈0.70 eV.

Second, the conductivity of the near-zero strain state heterostructures matches well with values measured for bulk single-crystal samples (e.g., the conductivity at 600 °C for our films and bulk samples are 0.0126 and 0.0128 S cm^{-1},[8] respectively). Third, the structural changes in LSGM are revealed to have a significant impact on the ion-transport properties. In particular, from compressive strain to near-zero strain, as the LSGM unit-cell volume increases by ≈1% and the octahedral-rotation magnitude remains almost invariant, the conductivity of the LSGM is increased by ≈100%, indicating that a larger unit-cell volume is preferred to achieve high ionic conductivity. Moreover, as the unit-cell volume is further increased by another ≈1% under tensile strain, while simultaneously quenching the octahedral rotations, the observed conductivity is negligibly affected (increases by <5%, within the error bars of the measurement). This suggests that quenching the octahedral rotations also strongly affects the overall transport properties, thus counterbalancing the effect of the expanded unit cell (UC) under tensile strain. In other words, this suggests that to achieve high ionic conduction in perovskite structures, the material should be controlled to have both larger unit-cell volume and octahedral rotations.

To understand why these structural features impact ionic conductivity in this manner, we applied DFT calculations coupled with a Green's function method[37] to probe the local effect of structure on ion transport (Experimental Section). We will first discuss the effect of octahedral rotations on ionic transport and then address the impact of volume change. The undoped $LaGaO_3$ parent phase was examined to study the impact of octahedral rotations on ion-migration pathways, and at the same time to eliminate dopant-strain effects. Because of the distorted octahedra in $LaGaO_3$, there are two distinct oxygen sites located either in the LaO or GaO_2 planes, denoted as O1 and O2, respectively (**Figure 3**a and Figure S8a, Supporting Information). Calculations further support this difference in that the energy of a vacancy at an O1 site is 15 meV lower than that for a vacancy at an O2 site. Furthermore, due to the octahedral rotations,[38,39] it is found that there are two O1–O1-type and four O1–O2-type symmetry-unique vacancy jumps with distinct migration-energy barriers (noted in various colors, Figure 3a, bottom). Since there are no allowed O2–O2-type jumps, vacancy migration along the three orthogonal axes (i.e., in-plane [001] and [1$\bar{1}$0], and out-of-plane [110]) is achieved by either a series of O1–O1-type or a combination of O1–O1 and O1–O2-type jumps. As a result, compared to a cubic system with no octahedral rotations, the presence of octahedral rotations creates different energy barriers to ion migration along each direction and, in turn, anisotropic jump phenomena. Thus, ion conduction preferentially occurs along a sub-set of low-energy jumps thereby resulting in two types of fast ion-conducting pathways: The first is via a series of O1–O1-type jumps (two equivalent pathways along different directions are shown, Figure 3b) and the second is via a series of O1–O1 and O1–O2-type jumps (Figure 3c). In general, the O1–O1-type jump with the highest energy (0.35 eV) determines the overall migration-energy barrier. We note that this value is smaller than that extracted from the experiments (≈0.70 eV) and this discrepancy

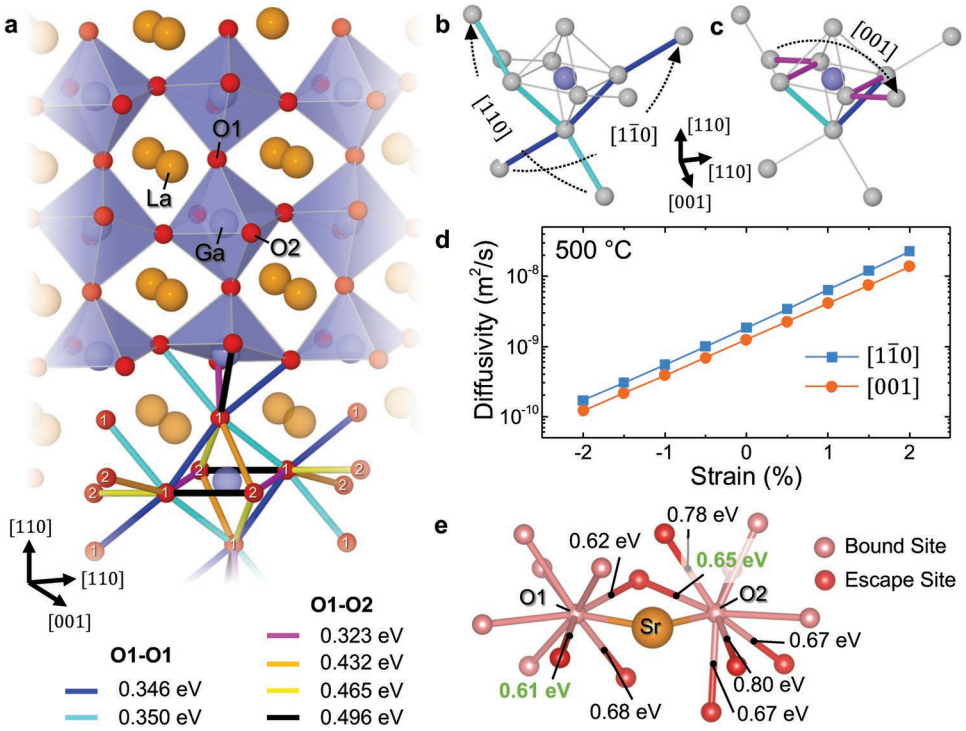

Figure 3. First-principles study of oxygen vacancy migration in LSGM. a) Illustration of the undoped $LaGaO_3$ crystal from the DFT calculations (top). Calculations further reveal six unique energy barriers for different oxygen vacancy jumps (each jump is labeled with different color, bottom). The values of migration barriers are given relative to the O1 site and there are two O1–O1 and four O1–O2-type jumps. b,c) Schematic illustrations of various fast ion-conducting oxygen vacancy migration pathways including ones based on a series of O1–O1-type jumps (two equivalent pathways along different directions are shown) (b), and one based on a series of O1–O1 and O1–O2-type jumps (c). d) DFT-calculated vacancy diffusivity as a function of strain for undoped $LaGaO_3$. e) Migration energies for oxygen vacancies when $LaGaO_3$ is doped with strontium at lanthanum sites where vacancies are found to either jump between bound sites (i.e., circle around the strontium trap) through low-energy barrier jumps (0.20–0.45 eV) or jump toward unbound sites (i.e., escape from the strontium trap) through high-energy barrier jumps (0.61–0.80 eV).

will be addressed later. Having established the effect of octahedral rotations on ionic migration, biaxial strain (compressive −2% to tensile +2%) was subsequently applied to examine the impact of unit-cell volume change. In undoped $LaGaO_3$, the unit-cell volume is shown to expand by ≈8% from compressive to tensile strain while the octahedral rotations remain almost unchanged (<2° change in angles across this entire range of strain; Figure S8b, Supporting Information), and therefore the impact of unit-cell volume can be isolated. Diffusivity calculations reveal that, from compressive to tensile strain, the vacancy diffusivity increases almost linearly across the experimentally probed regime from −1% to 1% strain (Figure 3d). This enhancement of the diffusivity is a direct consequence of a reduction of the migration-energy barriers across that strain regime (Figure S8c, Supporting Information). We note that the exact computation of diffusivity in LSGM is not a trivial matter and requires mesoscopic modeling approaches;[21,40,41] this said, the DFT results support the trends of the experimental findings wherein a larger unit-cell volume enables enhanced ionic conduction, consistent with prior works on ion-conducting materials.[15,17,42–45]

For a better representation of the experimental scenario, both strontium- and magnesium-doped versions of $LaGaO_3$ were also examined by DFT. These studies reveal that the nearest strontium-on-lanthanum sites (Sr_1) have attractive binding with both vacancy sites (O1 and O2) while the nearest magnesium-on-gallium sites (Mg_1) have negligible repulsive binding with the vacancies (Figure S9a,b, Supporting Information). In contrary to previous studies that suggested magnesium as the trapping center,[46] our results and recent studies[47,48] reveal that it is the strontium that attracts vacancies while magnesium does not. In turn, to examine the rate-limiting steps for vacancy diffusion, the oxygen-vacancy-migration barriers out of the most strongly bounded O1-Sr_1 and O2-Sr_1 vacancy configurations were calculated (Figure 3e). Vacancies are found to either jump between bound sites (i.e., circle around the strontium trap) through low-energy barrier jumps (0.20–0.45 eV) or jump toward unbound sites (i.e., escape the strontium trap) through high-energy barrier jumps (0.61–0.80 eV). In other words, vacancies are trapped inside a superbasin surrounding the strontium ions. The energies required for the vacancy to escape out of the superbasin, therefore, are likely to control the diffusion behavior. With the inclusion of dopant effects, the escape energies from O1 and O2 sites (0.61 and 0.65 eV) agree well with the experimentally observed activation barriers (≈0.70 eV). As the strontium concentration increases, however, these superbasins could overlap, leading to fast vacancy jumps between them (i.e., effectively a percolation effect with an overall fast diffusion rate). Once again, now building from both experimental and theoretical findings, the optimal design for high ion-conducting

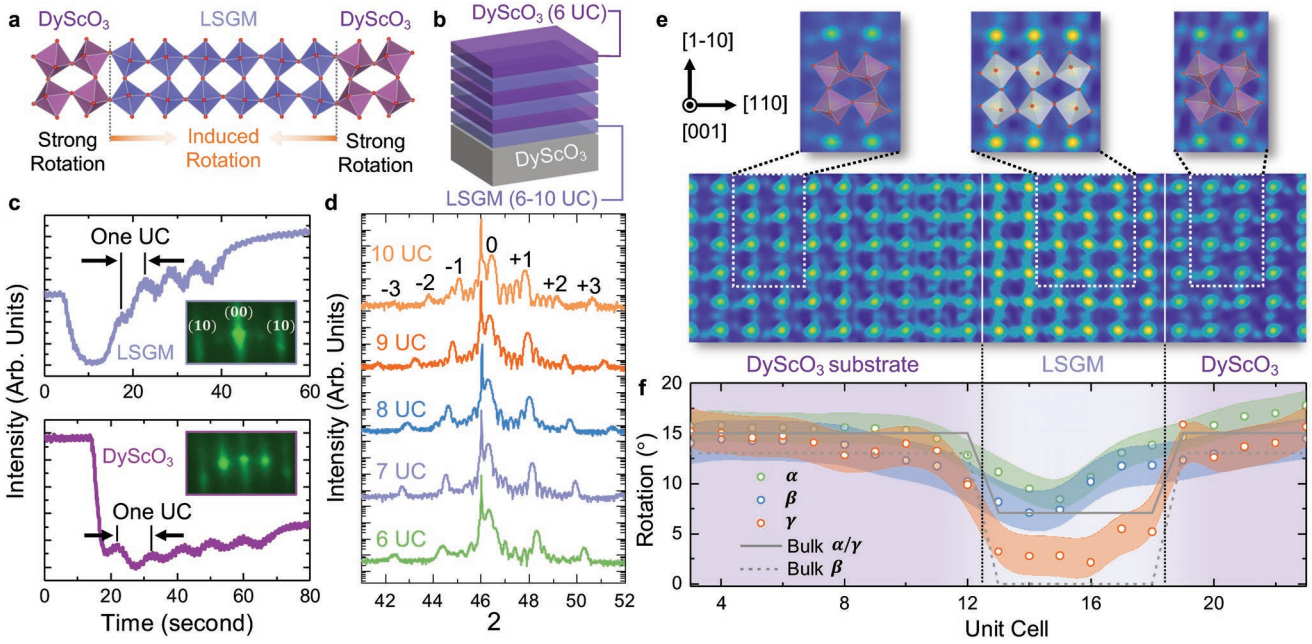

Figure 4. Creating the optimal structure for high ionic conductivity. a) Illustration of the introduction of octahedral rotations in an ultrathin film via interfacial engineering. b) Schematic of the $(LSGM)_n/(DyScO_3)_m$ superlattice structures. c) Reflection high-energy electron diffraction (RHEED) spectra for (top) LSGM and (bottom) $DyScO_3$ growth on $DyScO_3$ substrates; both films exhibit layer-by-layer growth. The insets show the sharp electron-diffraction patterns during growth, which reveal high surface quality and crystallinity. d) X-ray diffraction line scans for superlattice structures with $n = 6$–10 and $m = 6$ reveal clear Laue thickness fringes and superlattice peaks, indicating good crystallinity and sharp interfaces. e) Reconstructed electron density map for a $(DyScO_3)_6/(LSGM)_6/DyScO_3$ heterostructure from the COBRA analysis. The map reveals large octahedral rotations extending from the $DyScO_3$ into the ultrathin LSGM. f) Extracted octahedral rotation angles as a function of unit cell through the thickness of the heterostructure confirming the large octahedral rotation of both the bottom and top $DyScO_3$ layers and the formation of large in-plane rotations (α and β angles) in the LSGM that are markedly different from bulk values (solid and dashed lines).

perovskites is to combine large unit-cell volume and octahedral rotations.

As such, we now turn our attention to creating such an optimal structure wherein we can demonstrate the efficacy of this design process. To do this, we turn to a combined strain and interfacial engineering approach.[28,49] Although a particular rotation pattern of an epitaxial film is energetically fixed under a given strain state,[50,51] it has been shown that utilization of perovskite substrates with large octahedral rotations can drive an increase in the rotation magnitude in the film near the heterointerface (**Figure 4**a).[28,49,52,53] Thus, in order to achieve both large unit-cell volume and octahedral rotations in the LSGM, we turn to superlattice $(DyScO_3)_m/(LSGM)_n$ structures (where m and n refer to the number of UCs of $DyScO_3$ and LSGM, respectively) grown on $DyScO_3$ substrates (Figure 4b). The superlattice structure is chosen for a number of reasons. First, $DyScO_3$ is an insulating material with large octahedral rotations (the scandium–oxygen–scandium bonding angle is ≈140°)[54,55] such that the rotation pattern from the $DyScO_3$ interlayers can propagate into the LSGM layers. Second, $DyScO_3$ substrates are chosen to maintain the desired tensile strain to expand the unit-cell volume of the LSGM. Finally, multiple LSGM layers give rise to higher total conductance to limit the substrate contribution to the measured conductance and facilitate easier measurement of the ion-transport properties.

$(DyScO_3)_m/(LSGM)_n$ superlattices (m = 6 UC, n = 6–10 UC) were prepared via reflection high-energy electron diffraction (RHEED) assisted pulsed-laser deposition (Figure 4c). X-ray diffraction studies reveal strong superlattice peaks with clear Laue fringes, indicating high crystallinity and sharp interfaces (Figure 4d); features further validated by sharp in situ RHEED patterns during growth (insets in Figure 4c). The superlattices are found to be coherently strained to the substrate via reciprocal space mapping studies (Figure S10a, Supporting Information) and structurally and chemically robust during ≈24 h of high-temperature measurement (Figure S10b, Supporting Information). To confirm the realization of the desired large unit-cell volume and octahedral rotations in the LSGM, synchrotron-based X-ray crystal truncation rod (CTR) measurements accompanied by coherent Bragg rod analysis (COBRA) were performed on a 6 UC $DyScO_3$/6 UC LSGM/$DyScO_3$ (110) heterostructure emulating a single repeat of the superlattices. COBRA allows for the extraction of atomic positions for each layer near the surface (top ≈20 nm).[56] Although the rotation magnitude of thicker LSGM films under tensile strain is nearly zero, the electron density maps projected along the [001] (projection along $[1\bar{1}0]$ is also provided; Figure S10c, Supporting Information) reveal large tilts of the octahedra in the embedded LSGM layer (Figure 4e). Both $DyScO_3$ layers also show large and rigid octahedral-rotation patterns, with rotation angles in good agreement with bulk.[54,55] The extracted octahedral rotations for the LSGM layer are, however, drastically different from bulk[33] (Figure 4f). Namely, the two in-plane rotation angles (α and β) are increased due to the coupling with the $DyScO_3$ layers while the out-of-plane rotation angle (γ) is quenched as a result of the tensile strain. Overall, compared to the 100 nm

thick LSGM grown directly on $DyScO_3$ substrates where the octahedral rotations are significantly quenched, the effective octahedral-rotation magnitude for the ultrathin LSGM in the superlattice structures has been dramatically increased from ≈2.3° to ≈13.7°.

Having demonstrated that the superlattice produces the desired effect on the crystal structure, impedance measurements were completed (Figure S11a, Supporting Information). To accurately extract the ionic conductivity of this optimal structure in the superlattice geometry, we have two challenges: the first is to assure that all LSGM layers are similarly conducting and the second is to have accurate values of the thickness of the conducting layers. To accomplish this, we take advantage of our ability to grow various superlattice structures and periodicities to apply standard scaling laws to the analysis. To confirm that all LSGM layers were conducting and to rule out conductivity contribution from the $DyScO_3$, we examined multiple heterostructures built from a single representative $(DyScO_3)_6/(LSGM)_6$ superlattice unit with different total film thickness (specifically in structures with 8 and 16 total repetitions) and it was found that the normalized resistance per LSGM layer was the same (Figure S10b, Supporting Information). In addition, measurements on a 30 nm $DyScO_3/DyScO_3$ heterostructure revealed that the $DyScO_3$ films are insulating (Figure S10d, Supporting Information). Together with the fact that the $DyScO_3$ interlayers have identical crystal structures as the $DyScO_3$ substrates as revealed by COBRA data, we believe it is reasonable to claim that the $DyScO_3$ interlayers do not contribute to the total conductivity. As it pertains to understanding the thickness of the conducting layers, because there is a lack of complete understanding about the nature of ionic conduction at and near interfaces, we make no assumption that each of the LSGM unit cells is conducting in the same fashion. In turn, we assume the average resistance of each conducting LSGM unit cell to be R_{UC} and recalling that the total number of LSGM unit cells is n, the number of conducting LSGM unit cells will be $n - \Delta$, where Δ denotes potentially nonconducting unit cells at or near interfaces (Figure S11c, Supporting Information). As such, a linear relationship between the resistance per layer R_L and n is expected $[R_L^{-1} = R_{UC}^{-1}(n - \Delta)]$. Fitting this relation across the temperature region of interest (500–650 °C) by merely varying n yields R_{UC} and subsequently the conductivity of the conducting unit cells of LSGM can be extracted (Figure S11e,f, Supporting Information). We observe an invariant number of nonconducting LSGM "dead layers" ($\Delta \approx 5$) across all superlattice structures. One potential explanation for this is strontium enrichment near the top of the LSGM layers, observed by low-energy ion scattering (Experimental Section and Figure S12a,b, Supporting Information), which could disturb the local strain, exacerbate trapping, and impede migration.[12,57] With this noted, we extracted the conductivity of our optimized perovskite structure and find that it is increased by a factor of ≈2.5 as compared to the nonoptimal, compressively strained heterostructures, and nearly 0.7 times as compared to the bulk-like state around 600 °C (**Figure 5** and Figure S11g, Supporting Information). This result suggests that the design algorithm revealed by this work can provide a pathway to enhance the ionic-transport properties.

In summary, the correlation between structural features (i.e., unit-cell volume and octahedral rotations) and ionic conductivity in perovskite oxides has been investigated. Quantifiable control over unit-cell volume and octahedral rotations in LSGM was achieved via strain engineering. It was found that unit-cell volume and octahedral rotations both have significant impact on ionic migration in the perovskite structure and the optimal design is to have both large unit-cell volume and octahedral rotations. DFT calculations of vacancy diffusion further reveal that larger unit-cell volume reduces migration-energy barriers while large octahedral rotations create low-energy migration pathways. Subsequent superlattice structuring enables the creation of both large unit-cell volume and octahedral rotations, which results in an enhancement of the conductivity. Again, this work reveals the detailed relationships between structural parameters and transport evolution in perovskite ion-conducting systems and provides insights toward a rational-design approach of electrolyte materials for intermediate-temperature energy conversion applications.

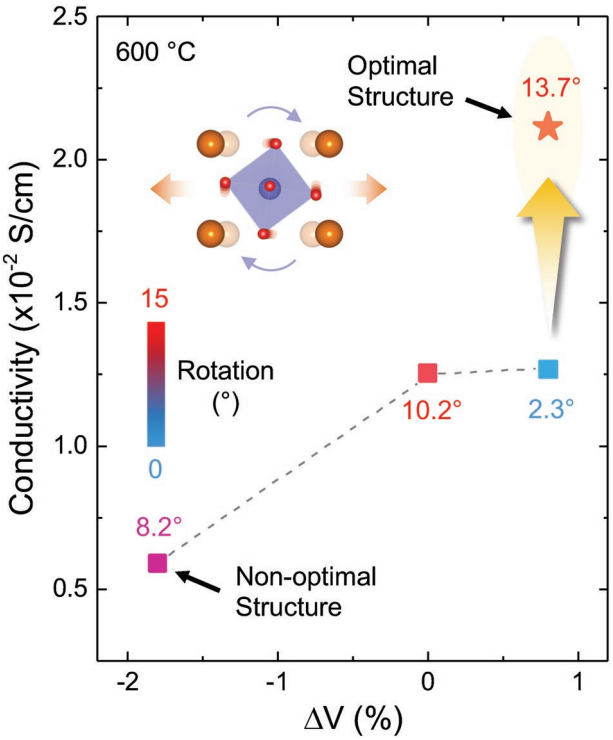

Figure 5. Enhanced conductivity in optimal LSGM. Ionic conductivity as a function of unit-cell volume and octahedral rotation angles for LSGM at 600 °C. Upon superlattice structuring the tensile-strained material (with the largest unit-cell volume) we can induce large octahedral rotations that drive an enhancement in the octahedral rotation angle and, correspondingly, the ionic conductivity.

Experimental Section

Thin-Film Synthesis: A ceramic target of $La_{0.9}Sr_{0.1}Ga_{0.9}Mg_{0.1}O_{3-\delta}$, with 95% theoretical density, was used for film growth. 100 nm thick LSGM thin films were grown via PLD on $NdGaO_3$ (110), $SrTiO_3$ (001), and $DyScO_3$ (110) substrates (CrysTec, GmBH). The LSGM films were grown at a heater temperature of 800 °C in a dynamic oxygen pressure of 40 mTorr and with a laser fluence and repetition rate of 1.8 J cm^{-2} and 5 Hz, respectively. All films were grown in an on-axis geometry with a

target-to-substrate distance of 52 mm. Following growth, the films were cooled to room temperature at a rate of 10 °C min^{-1} in a static oxygen pressure of 700 Torr. RHEED-assisted PLD was used to synthesize the superlattice structures. The same growth conditions were used for both the LSGM and $DyScO_3$ layers except that the laser repetition rate was adjusted to 2 and 3 Hz, respectively, for better visualization of the RHEED oscillations.

X-ray Diffraction Studies: A high-resolution X-ray diffractometer (Panalytical, X'Pert^3 MRD) was used to perform line scans and reciprocal space mapping studies about the 013_{pc} and 103_{pc}-diffraction conditions for cubic substrates and 332 and 420-diffraction conditions for orthorhombic substrates. Strain-dependent and high-temperature synchrotron-based X-ray half-order Bragg peak analysis was conducted at the Advanced Photon Source, Argonne National Laboratory, Sector 33-ID-D and Sector 33-BM-C, respectively. "Odd–odd–odd, odd–odd–even" and "odd–even–even" types of half-order peaks were systematically scanned in all four quadrants in reciprocal space and the peak intensities are integrated and corrected according to instrumental geometry. The peak intensities were subsequently fitted using an established approach for *Pbnm* perovskites and the octahedral rotation patterns and angles were extracted.[30] COBRA studies were completed at the Advanced Photon Source, Argonne National Laboratory, Sector 12-ID-D. CTRs were measured using a surface X-ray diffraction χ-geometry with a five-circle diffractometer under X-ray photon energy of 20 keV with a total flux of $\approx 2.0 \times 10^{12}$ photons s^{-1}. The 2D diffraction images of the CTRs at each L step in reciprocal space were recorded with a pixel array area detector (Dectris PILATUS 100 K). Samples were protected under dry helium gas flow in a concealed sample cell during room temperature measurements. A large set of CTRs in the reciprocal lattice coordinate was measured for 6 UC $DyScO_3$/6 UC LSGM/$DyScO_3$ (110) heterostructures at room temperature with $H_{max} = \pm 4$ RLU, $K_{max} = 4$ RLU, and $L_{max} = 9$ RLU under $2 \times 2 \times 2$ pseudocubic notation. This CTR data set included all relevant superstructure Bragg rods due to the oxygen octahedral rotation and *A*-site cation displacement off the symmetric point.[56]

Rutherford Backscattering Spectrometry: The film chemistry was probed ex situ using Rutherford backscattering spectrometry (incident ion energy 3.3 MeV, incident angle $\alpha = 22.5°$, exit angle $\beta = 25.35°$, and scattering angle $\theta = 168°$) and the spectra were fitted using the RBS analysis software SIMNRA. The beam energy was specifically tuned around magnesium resonance to maximize the scattering cross section for this light element.[58]

Impedance-Spectroscopy Studies: Impedance studies were completed with a PARSTAT 3000A Potentiostat (Princeton Applied Research) and impedance spectra were fitted using ZView software (Solartron Analytical). Transport measurements were performed by sputtering 120 nm thick platinum interdigitated electrodes (8 µm spacing, 500 µm arm length) and subsequently gold-wire-bonded to a Ceramic Dual In-line Package (CerDIP, TopLine Corp.) chip carrier. Samples were sealed inside an alumina tube. Electrical connections from CerDIP to the customized feedthroughs at one end of the tube were made via silver wires electrically/thermally insulated by ceramic beads. A *K*-type thermocouple was mounted on the CerDIP and wired out from the customized feedthrough for temperature readout. To achieve different oxygen partial pressures, the alumina tube was first pumped down to vacuum and then flushed with oxygen or nitrogen gas (Praxair Inc.) with 99.99% purity. A constant oxygen or nitrogen gas flow, with flow rate of 30 mL min^{-1} (monitored by two separate flowmeters), was maintained during measurement.

Density-Functional Theory: The DFT calculations were performed using Perdew–Burke–Ernzerhof (PBE) exchange-correlation functional and the projector augmented wave (PAW) method implemented in Vienna Ab Initio Simulation Package (VASP). Lanthanum, strontium, gallium, magnesium, and oxygen atoms were described with electronic structure $5s^2 5p^6 5d^1 6s^2$, $4s^2 4p^6 5s^2$, $3d^{10} 4s^2 4p^1$, $2p^6 3s^2$, and $2s^2 2p^4$, respectively. A plane wave energy cut-off of 500 eV was used to converge the total energy of the $LaGaO_3$ unit cell to below 1 meV per atom. The supercell of $LaGaO_3$ consisted of 160 atoms with a size of $2 \times 2 \times 2$ and required a Monkhorst–Pack *k*-point mesh size of $4 \times 4 \times 2$ to sample the Brillouin zone. The density of states was integrated via Gaussian smearing with an energy smearing width of 0.2 eV. The convergence criterion for electronic minimization was an energy difference smaller than 10^{-8} eV and the geometries were relaxed using conjugate gradient until the force on each atom was less than 5 meV $Å^{-1}$. Climbing image nudged elastic band (NEB) method with a single image was used to determine the transition states for vacancy jumps. The diffusivities were obtained using a recently developed analytical Green function approach,[37] which can be found at https://github.com/DallasTrinkle/Onsager. The Green function approach required the vacancy-jump network, the site energies for all unique sites in the network, and the transition rates for all unique jumps within the network as input parameters. Each transition rate had the Arrhenius form of $Ae^{-E/kT}$, where E is the migration barrier and A is the attempt frequency. The migration barrier was the difference between the transition state energy and the initial state energy. For both the strained and unstrained geometries, the site and transition state energies were obtained from zero Kelvin DFT calculations that considered single-vacancy hops in an undoped $LaGaO_3$ supercell. The attempt frequency accounted for the entropy contributions to the transition rate. The attempt frequencies were calculated by approximating the Vineyard expression using only the real vibrational frequencies of the jumping atom in the initial and the transition state.

Supporting Information

Supporting Information is available from the Wiley Online Library or from the author.

Acknowledgements

R.G., A.C.P.J., A.L., E.E., N.H.P., and D.R.T. acknowledge the support of the National Science Foundation under grant OISE-1545907. S.P. acknowledges support of the Army Research Office under grant W911NF-14-1-0104. Y.D. and H.Z. acknowledge the used resources of the Advanced Photon Source, a U.S. Department of Energy (DOE) Office of Science User Facility operated for the DOE Office of Science by Argonne National Laboratory under Contract No. DE-AC02-06CH11357. L.R.D., Y.Y., and V.G. acknowledge the support of the U.S. Department of Energy, Office of Science, Office of Basic Energy Sciences, under Award Number DE-SC-0012375 for development of the complex-oxide materials and chemical studies herein and the COBRA analysis. V.T. and T.I. acknowledge the financial support from a Grant-in-Aid for Specially Promoted Research (No.16H06293) from MEXT, Japan and through the Japan Society for the Promotion of Science and the Solid Oxide Interfaces for Faster Ion Transport JSPS Core-to-Core Program (Advanced Research Networks). S.S. acknowledges support of the National Science Foundation under grant DMR-1608938. R.X. acknowledges support from the National Science Foundation under grant DMR-1708615. T.C. acknowledges a JSPS doctoral fellowship. N.H.P. and T.C. also acknowledge the support of the International Institute for Carbon Neutral Energy Research (WPI-I2CNER), sponsored by the Japanese Ministry of Education, Culture, Sports, Science and Technology. L.W.M. acknowledges support from the U.S. Department of Energy, Office of Science, Office of Basic Energy Sciences, Materials Sciences and Engineering Division under Contract No. DE-AC02-05-CH11231: Materials Project program KC23MP for development of functional complex-oxide materials. The computational work used the Extreme Science and Engineering Discovery Environment (XSEDE), which is supported by National Science Foundation grant number ACI-1053575.

[1] B. C. H. Steele, A. Heinzel, *Nature* **2001**, *414*, 345.
[2] R. Scataglini, M. Wei, A. Mayyas, S. H. Chan, T. Lipman, M. Santarelli, *Fuel Cells* **2017**, *17*, 825.
[3] O. Yamamoto, *Electrochim. Acta* **2000**, *45*, 2423.
[4] E. D. Wachsman, K. T. Lee, *Science* **2011**, *334*, 935.
[5] Z. Gao, L. V. Mogni, E. C. Miller, J. G. Railsback, S. A. Barnett, *Energy Environ. Sci.* **2016**, *9*, 1602.
[6] T. Ishihara, H. Matsuda, Y. Takita, *J. Am. Chem. Soc.* **1994**, *116*, 3801.
[7] T. Ishihara, N. P. Bansal, in *Perovskite Oxide Solid Oxide Fuel Cells* (Ed: T. Ishihara), Springer, Boston, MA, USA **2009**, pp. 65–93.
[8] G. M. Rupp, M. Glowacki, J. Fleig, *J. Electrochem. Soc.* **2016**, *163*, F1189.
[9] M. Li, M. J. Pietrowski, R. A. De Souza, H. Zhang, I. M. Reaney, S. N. Cook, J. A. Kilner, D. C. Sinclair, *Nat. Mater.* **2014**, *13*, 31.
[10] M. Li, H. Zhang, S. N. Cook, L. Li, J. A. Kilner, I. M. Reaney, D. C. Sinclair, *Chem. Mater.* **2015**, *27*, 629.
[11] M. Filal, C. Petot, M. Mokchah, C. Chateau, J. L. Carpentier, *Solid State Ionics* **1995**, *80*, 27.
[12] K. Huang, R. S. Tichy, J. B. Goodenough, *J. Am. Ceram. Soc.* **2005**, *81*, 2565.
[13] T. Mori, J. Drennan, J. H. Lee, J. G. Li, T. Ikegami, *Solid State Ionics* **2002**, *154–155*, 529.
[14] A. Cheikh, A. Madani, A. Touati, H. Boussetta, C. Monty, *J. Eur. Ceram. Soc.* **2001**, *21*, 1837.
[15] J. L. M. Rupp, *Solid State Ionics* **2012**, *207*, 1.
[16] C. Korte, A. Peters, J. Janek, D. Hesse, N. Zakharov, *Phys. Chem. Chem. Phys.* **2008**, *10*, 4623.
[17] J. Jiang, X. Hu, W. Shen, C. Ni, J. L. Hertz, *Appl. Phys. Lett.* **2013**, *102*, 143901.
[18] K. Mohan Kant, V. Esposito, N. Pryds, *Appl. Phys. Lett.* **2012**, *100*, 033105.
[19] N. Schichtel, C. Korte, D. Hesse, N. Zakharov, B. Butz, D. Gerthsen, J. Janek, *Phys. Chem. Chem. Phys.* **2010**, *12*, 14596.
[20] J. Garcia-Barriocanal, A. Rivera-Calzada, M. Varela, Z. Sefrioui, E. Iborra, C. Leon, S. J. Pennycook, J. Santamaria, *Science* **2008**, *321*, 676.
[21] M. Saiful Islam, *J. Mater. Chem.* **2000**, *10*, 1027.
[22] T. Mayeshiba, D. Morgan, *Phys. Chem. Chem. Phys.* **2015**, *17*, 2715.
[23] A. Kushima, B. Yildiz, *J. Mater. Chem.* **2010**, *20*, 4809.
[24] A. Marthinsen, C. Faber, U. Aschauer, N. A. Spaldin, S. M. Selbach, *MRS Commun.* **2016**, *6*, 182.
[25] R. A. De Souza, A. H. H. Ramadan, *Phys. Chem. Chem. Phys.* **2013**, *15*, 4505.
[26] H. Hayashi, H. Inaba, M. Matsuyama, N. G. Lan, M. Dokiya, H. Tagawa, *Solid State Ionics* **1999**, *122*, 1.
[27] M. Mogensen, D. Lybye, N. Bonanos, P. V. Hendriksen, F. W. Poulsen, *Solid State Ionics* **2004**, *174*, 279.
[28] R. Gao, Y. Dong, H. Xu, H. Zhou, Y. Yuan, V. Gopalan, C. Gao, D. D. Fong, Z. Chen, Z. Luo, L. W. Martin, *ACS Appl. Mater. Interfaces* **2016**, *8*, 14871.
[29] S. J. May, J. W. Kim, J. M. Rondinelli, E. Karapetrova, N. A. Spaldin, A. Bhattacharya, P. J. Ryan, *Phys. Rev. B* **2010**, *82*, 014110.
[30] M. Brahlek, A. K. Choquette, C. R. Smith, R. Engel-Herbert, S. J. May, *J. Appl. Phys.* **2017**, *121*, 045303.
[31] P. Slater, *Solid State Ionics* **1998**, *107*, 319.
[32] P. R. Slater, J. T. S. Irvine, T. Ishihara, Y. Takita, *J. Solid State Chem.* **1998**, *139*, 135.
[33] M. M. Guenter, M. Lerch, H. Boysen, D. Toebbens, E. Suard, C. Baehtz, *J. Phys. Chem. Solids* **2006**, *67*, 1754.
[34] J. Jamnik, J. Maier, *Phys. Chem. Chem. Phys.* **2001**, *3*, 1668.
[35] W. Lai, S. M. Haile, *J. Am. Ceram. Soc.* **2005**, *88*, 2979.
[36] R. A. De Souza, *Adv. Funct. Mater.* **2015**, *25*, 6326.
[37] D. R. Trinkle, *Philos. Mag.* **2016**, *96*, 2714.
[38] W. Marti, P. Fischer, F. Altorfer, H. J. Scheel, M. Tadin, *J. Phys.: Condens. Matter* **1994**, *6*, 127.
[39] C. J. Howard, B. J. Kennedy, *J. Phys.: Condens. Matter* **1999**, *11*, 3229.
[40] M. Cherry, M. S. Islam, C. R. A. Catlow, *J. Solid State Chem.* **1995**, *118*, 125.
[41] M. S. Islam, M. Cherry, C. R. A. Catlow, *J. Solid State Chem.* **1996**, *124*, 230.
[42] Y. Shi, A. H. Bork, S. Schweiger, J. L. M. Rupp, *Nat. Mater.* **2015**, *14*, 721.
[43] J. L. M. Rupp, E. Fabbri, D. Marrocchelli, J.-W. Han, D. Chen, E. Traversa, H. L. Tuller, B. Yildiz, *Adv. Funct. Mater.* **2014**, *24*, 1562.
[44] M. Kubicek, Z. Cai, W. Ma, B. Yildiz, H. Hutter, J. Fleig, *ACS Nano* **2013**, *7*, 3276.
[45] M. J. D. Rushton, A. Chroneos, S. J. Skinner, J. A. Kilner, R. W. Grimes, *Solid State Ionics* **2013**, *230*, 37.
[46] M. S. Khan, M. S. Islam, D. R. Bates, *J. Phys. Chem. B* **1998**, *102*, 3099.
[47] F. Blanc, D. S. Middlemiss, Z. Gan, C. P. Grey, *J. Am. Chem. Soc.* **2011**, *133*, 17662.
[48] M. Gambino, S. Di Tommaso, F. Giannici, A. Longo, C. Adamo, F. Labat, A. Martorana, *J. Chem. Phys.* **2017**, *147*, 144702.
[49] Z. Liao, M. Huijben, Z. Zhong, N. Gauquelin, S. Macke, R. J. Green, S. Van Aert, J. Verbeeck, G. Van Tendeloo, K. Held, G. A. Sawatzky, G. Koster, G. Rijnders, *Nat. Mater.* **2016**, *15*, 425.
[50] J. M. Rondinelli, N. A. Spaldin, *Phys. Rev. B* **2010**, *82*, 113402.
[51] A. Vailionis, H. Boschker, W. Siemons, E. P. Houwman, D. H. A. Blank, G. Rijnders, G. Koster, *Phys. Rev. B* **2011**, *83*, 064101.
[52] S. J. May, C. R. Smith, J. W. Kim, E. Karapetrova, A. Bhattacharya, P. J. Ryan, *Phys. Rev. B* **2011**, *83*, 153411.
[53] J. He, A. Borisevich, S. V. Kalinin, S. J. Pennycook, S. T. Pantelides, *Phys. Rev. Lett.* **2010**, *105*, 227203.
[54] B. Veličkov, V. Kahlenberg, R. Bertram, M. Bernhagen, *Z. Kristallogr.* **2007**, *222*, 466.
[55] T. Heeg, J. Schubert, C. Buchal, E. Cicerrella, J. L. Freeouf, W. Tian, Y. Jia, D. G. Schlom, *Appl. Phys. A* **2006**, *83*, 103.
[56] Y. Yuan, Y. Lu, G. Stone, K. Wang, C. M. Brooks, D. G. Schlom, S. B. Sinnott, H. Zhou, V. Gopalan, *Nat. Commun.* **2018**, *9*, 5220.
[57] S. Li, B. Bergman, *J. Eur. Ceram. Soc.* **2009**, *29*, 1139.
[58] H. Cheng, H. Shen, F. Yang, J. Tang, *Nucl. Instrum. Methods Phys. Res. B* **1994**, *85*, 47.